communications earth & environment **Article**

https://doi.org/10.1038/s43247-024-01774-0

Response of the upper ocean to northeast Pacific atmospheric rivers under climate change

Christine A. Shields [1,5] ✉, **Hui Li** [1,5], **Frederic S. Castruccio** [1], **Dan Fu** [2,3], **Kyle Nardi**[4], **Xue Liu**[2] & **Colin Zarzycki**[4]

Atmospheric rivers are important transport vehicles for Earth's water cycle. Using a high-resolution, eddy-resolving Earth System Model, atmospheric river impacts on the upper ocean are investigated by analyzing historical and climate change simulations. For atmospheric rivers along the North American coastline, strong winds cause significant dynamic and thermodynamic upper ocean responses. They push ocean water towards the coast, measured by sea surface height, a process that is amplified under climate change. Mixed layers are deeper upstream of atmospheric rivers, and shallower downstream, however for climate change, shoaling downstream is subdued. Air-sea heat fluxes tend to promote ocean cooling upstream and warming downstream, although different regions have different climate change heat flux signals. Southern California heat flux changes due to warming are driven by evaporative processes and strengthen the ocean responses seen in historical simulations. The regions north are primarily dominated by sensible heat flux changes and counter the historical patterns.

Atmospheric rivers (ARs) are essential components of Earth's hydrological cycle, over both ocean basins and land masses. The oft-cited Zhu and Newell[1] publication tells us that ARs account for approximately 90% of the water vapor transport in their long, narrow, and meandering footprints, by moving water from lower to higher latitudes, primarily from the mid-latitudes to the poles. Much of the attention thus far has been rooted in the atmosphere and land surfaces, and spanning AR physical properties and characteristics[2–7], their impacts[8–10], uncertainties[11–13], and the rich body of literature surrounding climate change[14–19]. Their ability to act alternatingly as beneficial "drought-busters"[20], to massively destructive flood producers[21,22], captures the interests of scientists and stakeholders alike. AR research began primarily with studies focused on landfalling events over the North American West, to Western Europe and the Iberian Peninsula, but has exploded in recent years to ARs worldwide in regions such as South Africa[23], Chile[24], Australia and New Zealand[25,26], Middle East[27], and East Pacific[28]. The emerging field of AR impacts on the cryosphere provides insights into high latitude AR interactions with sea ice[29–31] and ice sheets[32–36].

Less studied are feedbacks between ARs and the ocean. ARs are characterized by powerful winds and strong moisture transport, which can cause substantial momentum and heat flux variations at the ocean surface. To date, research has primarily been focused on the interactions between sea surface temperatures (SSTs) and ARs in models[37–40], observations[41], and hindcasts[42]. The buoy-based observational study[41], centered around the Northeast Pacific ARs, found that SSTs and upper ocean latent heat fluxes are closely linked and suggests that ocean impacts may play an important role in AR intensity. The hindcast study[42] applied the SKRIPS regional modeling system and showed that the coupled simulations have better skill representing boundary layer AR water vapor and transport compared to uncoupled simulations. The paucity of AR ocean feedback studies can be largely explained by the lack of high-resolution ocean data required to understand interactions on these weather scales, a point made by Shinoda et al.[43], one of the few studies (to date) evaluating ocean variability and air-sea fluxes beyond SSTs. Using a high resolution (1/12°) ocean reanalysis product and AR data collected during the CalWater field campaign, Shinoda et al.[43] illustrate the forcing ARs impose on upper ocean processes such as momentum and heat fluxes, mixed layer depth (MLD), and sea surface height (SSH), but for a relatively short sample period (2011–2015). While not explicitly focused on ARs, observations taken during DYNAMO[44,45] and SPURS-2[46–48], show that convective storm activity in the atmosphere can drive SST and sea surface salinity (SSS) anomalies in the ocean. Storms possessing strong surface winds, such as tropical[49–52] and extratropical[53,54] cyclones, have been shown to impact the upper ocean state through

---

[1]NSF National Center for Atmospheric Research, Climate and Global Dynamics Lab, Boulder, CO, USA. [2]Department of Oceanography, Texas A&M University, College Station, TX, USA. [3]Department of Atmospheric Sciences, Texas A&M University, College Station, TX, USA. [4]Department of Meteorology and Atmospheric Science, Pennsylvania State University, University Park, PA, USA. [5]These authors contributed equally: Christine A. Shields, Hui Li. ✉e-mail: shields@ucar.edu

processes such as flux extraction, turbulent mixing, and Ekman pumping[55,56]. More recently, remote sensing products have been used to capture the response of the upper ocean to extreme atmospheric phenomena[57] (and references therein). Given this expansive literature, it is expected that—even in the relative absence of AR-specific work—that such storms interact with the ocean through similar processes. Building upon our current understanding on the exchanges of wind, water, and heat between the atmosphere and ocean from studies such as these, we begin to assess AR-ocean feedbacks. Here, we further explore these themes by applying a high-resolution Earth System Model with ~1/10° ocean-mesoscale-eddy-resolving and ~1/4° atmosphere–land resolution capabilities to simulate both historical and future climate scenarios to assess not only AR impacts at present, but also under climate change. Utilizing high-resolution modeling is the cornerstone of this work and follows the current understanding that increased horizontal resolution improves the characterization, climatology, and variability of ARs[58,59], the underlying dynamics of North Pacific storm tracks[60], and impacts such precipitation extremes[16,61,62].

Results

Eddy-resolving ocean influences atmospheric moisture

High-resolution ocean simulations allow for features such as mesoscale ocean eddies and fronts to be resolved. Because the modeling system is fully coupled, the ocean eddies can then exert influence back to the atmosphere, as illustrated in the AR snapshot in Fig. 1a. In this case, water vapor acts as a de facto tracer of ocean eddies and is demonstrated clearly in the column integrated water vapor (IWV) atmospheric field in a sample timeslice. The fine features in Fig. 1a are not present in the lower, ~1° horizontal resolution (Fig. 1b) which applies the same version of the coupled model. Sample snapshots in Fig. 1 are representative of the experiments regarding AR visual features. While high horizontal resolution in the atmosphere improves aspects of the atmospheric solution[63,64], increasing ocean resolution, evident in the corresponding SSTs in Fig. 1c, d, provides much improved oceanic processes and air-sea interactions, thereby improving the coupled solution[59,65], including ARs and their impacts[58].

Ocean responses to ARs

The high-resolution coupled model is able to simulate realistic AR footprints over the Pacific Ocean, allowing the assessment of their impact over the upper ocean. In observations, Shinoda et al.[43] performed such an evaluation using high-resolution ocean reanalysis demonstrating the impact ARs on the upper ocean from the period of 2011–2015. Here, we leverage this study by performing compositing across CESM-HR simulations and find the model performs realistically, matching the AR response in spatial character and approximating similar magnitudes. Figure 2a, f, k illustrates the synoptic composites of the AR footprints (6-hourly snapshots), represented by total integrated column water, in the historical (1966–2005) simulation for each AR landfall region—Southern California (SOCAL), California (CAL), and Pacific Northwest (PNW), respectively. Subsequent panels in Fig. 2 show composite changes in SST, SSS, ocean MLD, and SSH before and after the AR passage, relative to the long-term climatology. AR

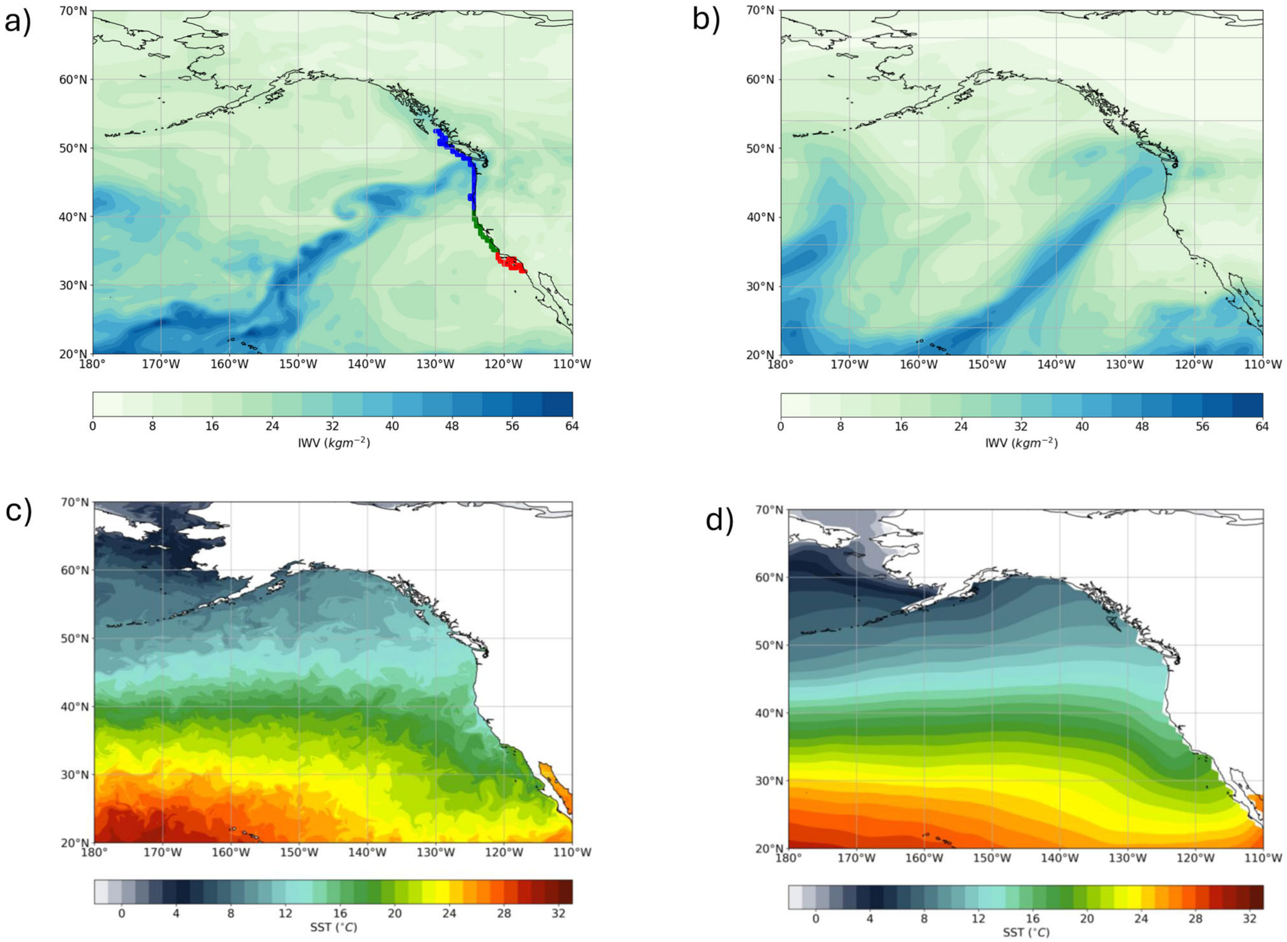

Fig. 1 | Comparing high versus standard resolution CESM. a Snapshot of Integrated Water Vapor (IWV) during an AR, simulated using the fully-coupled CESM1.3 model with 0.25° atmosphere and 0.1° ocean resolution (representative of ARs in this simulation). Regional areas described in this study are defined by the coastal locations where landfalling ARs occur, including Southern California (red circles), California (green circles, and Pacific Northwest (blue circles). **b** Snapshot of IWV during an AR simulated in CESM1.3 with 0.25° atmosphere and ~1° ocean resolution (representative of ARs in this simulation)[63,64]. **c** Daily mean sea surface temperature corresponding to (**a**). **d** Daily mean sea surface temperature corresponding to (**b**).

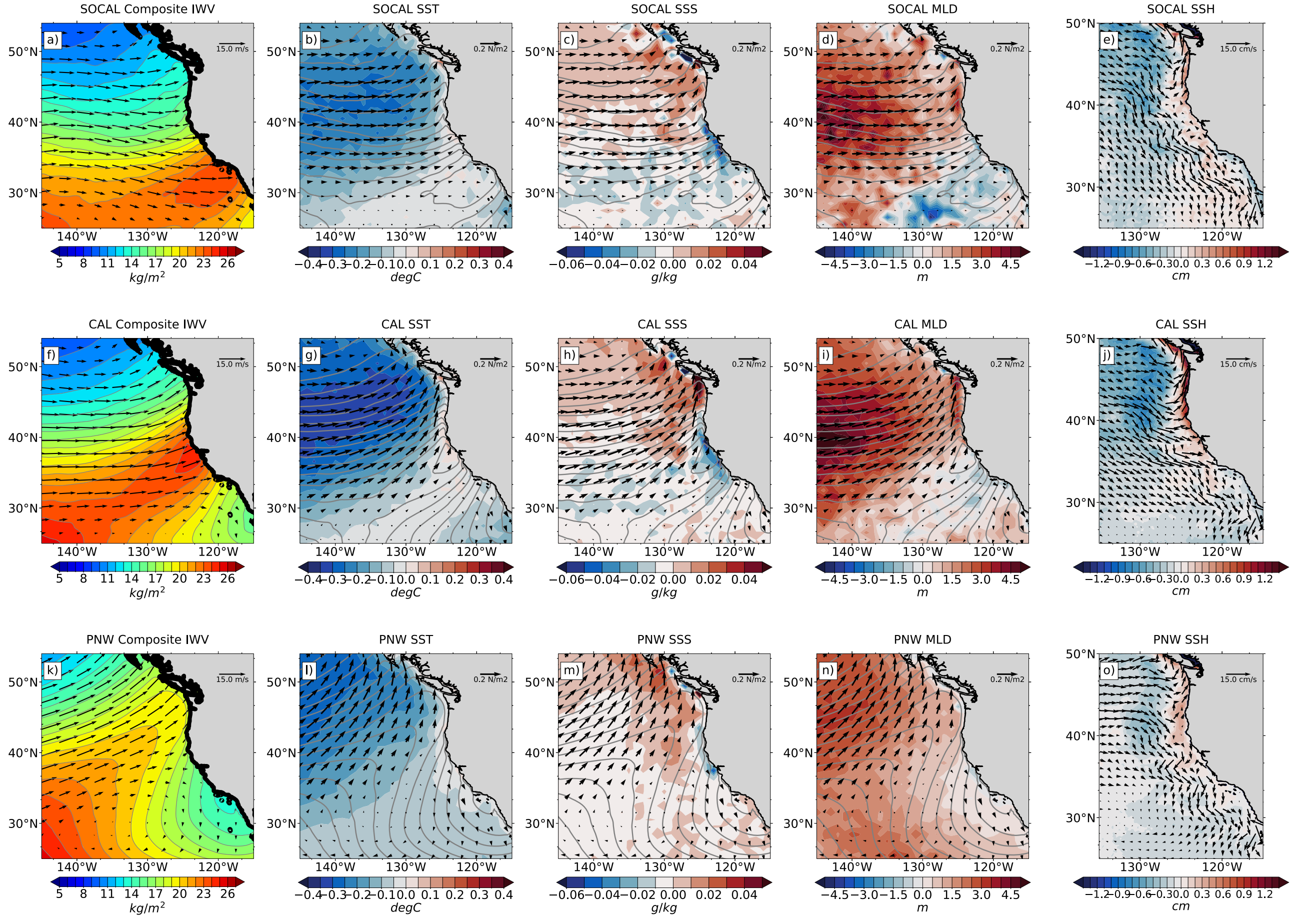

Fig. 2 | Sea surface temperature, salinity, mixed layer depth, and sea surface height responses to ARs for the historical period. Historical (1966–2005) anomaly composites for SOCAL (**a**–**d**), CAL (**e**–**h**) and PNW (**i**–**l**). IWV (**a**, **f**, **k**, kgm^{-1}), SST (**b**, **g**, **l**, °C), SSS (**c**, **h**, **m**), MLD (**d**, **I**, **n**, cm), and SSH (**e**, **j**, **o**, cm). 850 hPa wind vectors (ms^{-1}) are overlaid on IWV in (**a**, **e**, **f**), and surface wind stress vectors (Nm^{-2}) are overlaid on SST, SSS, and MLD. The panels (**e**, **j**, **o**) show the SSH and ocean surface current vectors (ms^{-1}) on the 0.1° model grid to show more details near the coastal region. Composites show ARDT consensus tracks. Anomalies are computed using 35-year long-term climatology using monthly means. IWV composite anomalies are shown as gray contours in each panel for location reference.

passage is defined as 3 days before onset and 3 days after, except for SSH which is computed with 1 day after passage. By removing the long-term climatology, the ocean base state is essentially removed thus leaving only the AR response itself and comparable to the ocean reanalysis reported in Shinoda et al.[43]. The MLD is expressed in terms of buoyancy, specifically the shallowest depth where the maximum gradient matches the local gradient[66]. Consensus ARs, i.e., only ARs where all atmospheric river detection tools (ARDTs) agree, are used. We apply three distinct ARDTs with different designs and levels of restrictiveness to encompass a wide range of AR definitions. (See methods for more details on ARDT, and our analysis technique, as well as the supplemental material for individual ARDT responses and context, Supplemental Table 1, Supplemental Figs. 1–4).

In all three AR regions, strong westerly low-level winds are present on the northwest side of AR upstreams, and tend toward southwesterly for the PNW. This is because ARs are often associated with an atmospheric frontal system that acts as a convergence zone along which the moisture is transported. The same region is characterized by substantial SST cooling (Fig. 2b, g, l) and mixed layer deepening (Fig. 2d, i, n). This indicates that strong wind forcing may directly contribute to both cooling and deepening by inducing enhanced turbulent heat flux exchange at the sea surface and shear-induced ocean vertical mixing (discussed in the next section). For SOCAL and CAL ARs, slight SST warming and MLD shoaling occur over the AR “center” (defined as the narrow band of maximum IWV) and downstream (southeast side). These regions correspond to weaker surface winds but higher humidity. For PNW ARs, the response is more diffuse and less pronounced, with no MLD shoaling and SST warming downstream (southeast quadrant of the plots). The effect of rainfall and SSS responses are shown in Figs. 2c, h, m and 3d, h, l. SSS is generally higher upstream of the AR passage, but lower along coastal regions which is mostly consistent with the maximum precipitation flux (Fig. 3). For SOCAL and CAL especially, there is also a clear signature of freshening along the AR northern boundary, which may increase upper ocean stratification and contribute to a reduction of the MLD (Fig. 2d, i, n). There may be competing effects between AR high wind and heavy rainfall on the upper ocean SST and MLD responses, which requires a comprehensive analysis of the ocean subsurface processes in future studies.

The sea level increases as wind stress pushes water towards the coastal regions, thereby producing higher values along the coast as water piles up at the land barrier. This is notable and important for coastal flooding and local communities. Model responses shown here are robustly consistent with observational analysis in Shinoda et al.[43] from both a case study and composite viewpoints (Shinoda Figs. 3–7) (See supplemental material for the model base states for ocean and ARs, Supplementary Figs. 5 and 6).

Figure 3 shows the composite anomalies of total surface heat flux (SHF), sensible heat flux (SENH), evaporative heat flux (EVAP), and precipitation flux into the ocean (PREC) corresponding to Fig. 2 (the convention is positive down). We find that SST anomalies (Fig. 2b, g, l) are largely correlated with the strong winds and the associated heat fluxes in and out of the upper ocean. On the northwest side of AR upstreams, stronger atmospheric winds induce increased surface wind stress, leading to SST cooling through enhancements of air-sea turbulent heat fluxes. The total surface heat loss is dominated by evaporative cooling (Fig. 3c, g, k) contributing up to 75% of heat loss for the CAL domains, though sensible

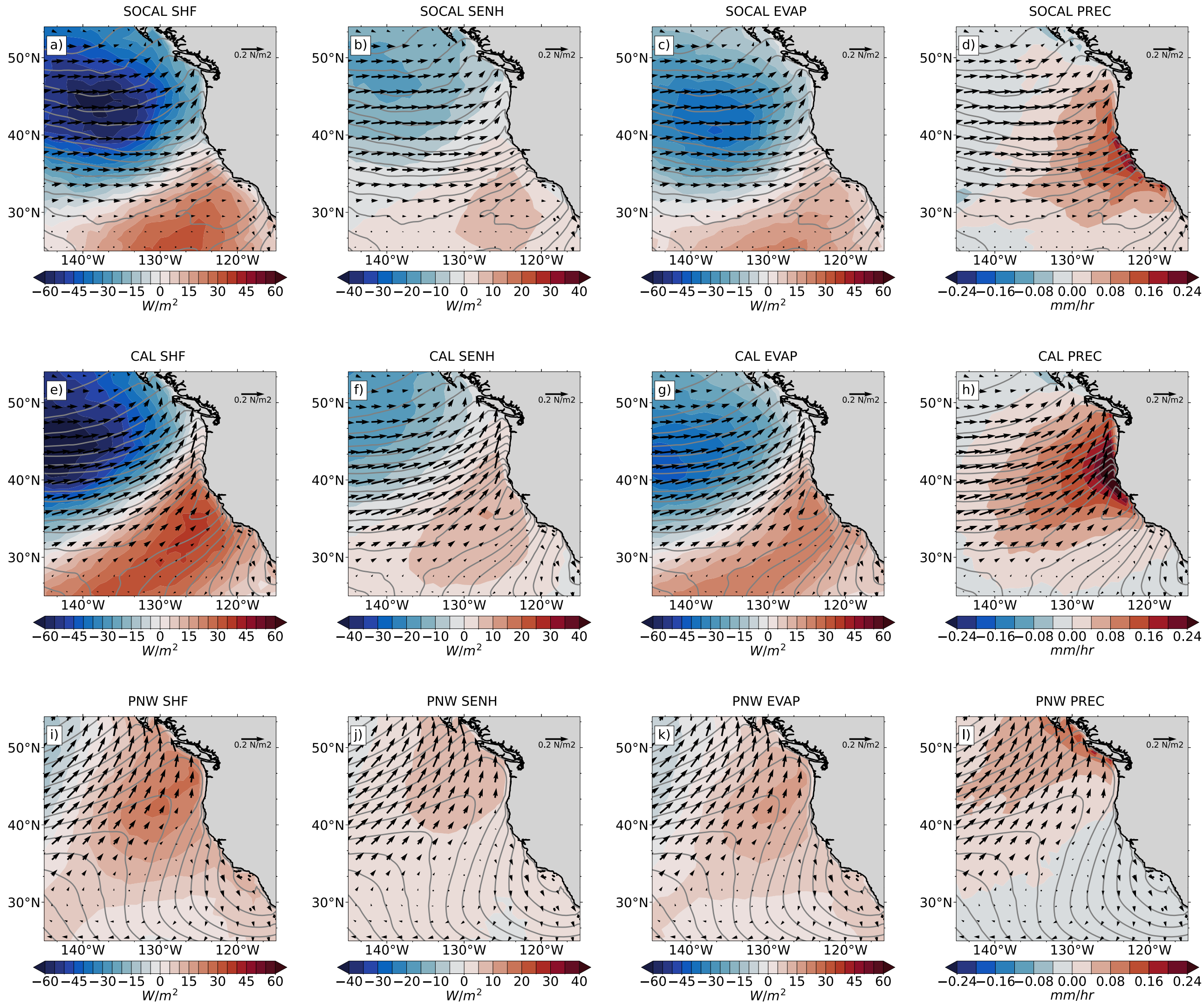

Fig. 3 | Ocean heat and precipitation flux responses to ARs for the historical period. Historical (1966–2005) heat flux and precipitation anomaly composites, for SOCAL (**a**–**d**), CAL (**e**–**h**), and PNW (**i**–**l**), with Fig. 2 methods. Total surface heat flux (SHF, **a**, **d**, **g**), sensible heat flux (SENH, **b**, **e**, **h**), evaporative heat flux (EVAP, **c**, **f**, **j**) (Wm^{-2}, respectively), and precipitation flux (mmh^{-1}) are plotted with wind stress vectors (Nm^{-2}). Positive values mean heat fluxes go downward into the ocean.

processes also contribute to the total changes. Downstream of ARs, SST warming and MLD shoaling occur under weaker winds and positive latent and SENHs into the ocean, consistent with the saturated boundary layer that is characteristic of ARs. Contribution from radiative fluxes is relatively small (not shown). The same basic mechanism is in play across all three regional locations, although in the PNW region, warming downstream of the ARs has a more robust response than the cooling upstream. The upper ocean responses and the associated turbulent flux changes are consistent with the observational analyses of AR upper ocean responses in ref. 43.

Climate change responses

Now that the fundamental ocean response to an AR passage has been established, we next examine potential signals under projected future warming. The Representative Concentration Pathway 8.5 (RCP8.5) represents the worst-case future RCP emission scenarios, and is used here to assess climate change impacts on AR-ocean feedbacks. The same analysis technique applied to the historical simulations is also repeated here, again noting the base state has been removed and only the AR response to climate change is shown. (See Supplementary Fig. 5 for the ocean base state and Supplementary Fig. 6 for the AR base state). Figure 4 shows the differences of AR composite responses between the future projections (2066–2100) and historical mean solutions. AR IWV significantly increases in all three regions. The most substantial changes are found in SOCAL, likely in part due to the predominance of "Pineapple Express" varieties that are only sometimes associated with extratropical systems[67]. This region is projected to experience a richer and narrower band of increased moisture (Fig. 4a, e, i). CAL and PNW ARs will more routinely co-occur with extratropical, cold core synoptic systems simply because they lie firmly in the storm track and mid-latitude westerlies[68–70]. IWV projections in these regions show a wider and less intense increase compared to SOCAL.

The upper ocean SST responses to projected warming vary across different regions. For SOCAL ARs, the upstream SST cooling increases under climate change. For CAL and PNW ARs, however, the upstream temperature change (particularly north of 40°N) is less pronounced. The differences in surface temperature responses can be largely explained by SHFs. Again, heat fluxes (Fig. 5) have a different climate change response in SOCAL compared to ARs impacting more northern latitudes. The evaporative component is far more dominant in SOCAL and accounts for almost all of the SHF signature reinforcing the dipole-like pattern of strong cooling upstream and warming downstream of the ARs. For example, averaging only the locales with significant changes, cooling upstream of SOCAL ARs is projected to be ~20 W/m^2 countered with warming downstream of ~17 W/m^2. However, changes to the CAL AR heat flux anomalies have almost the opposite signal compared to SOCAL

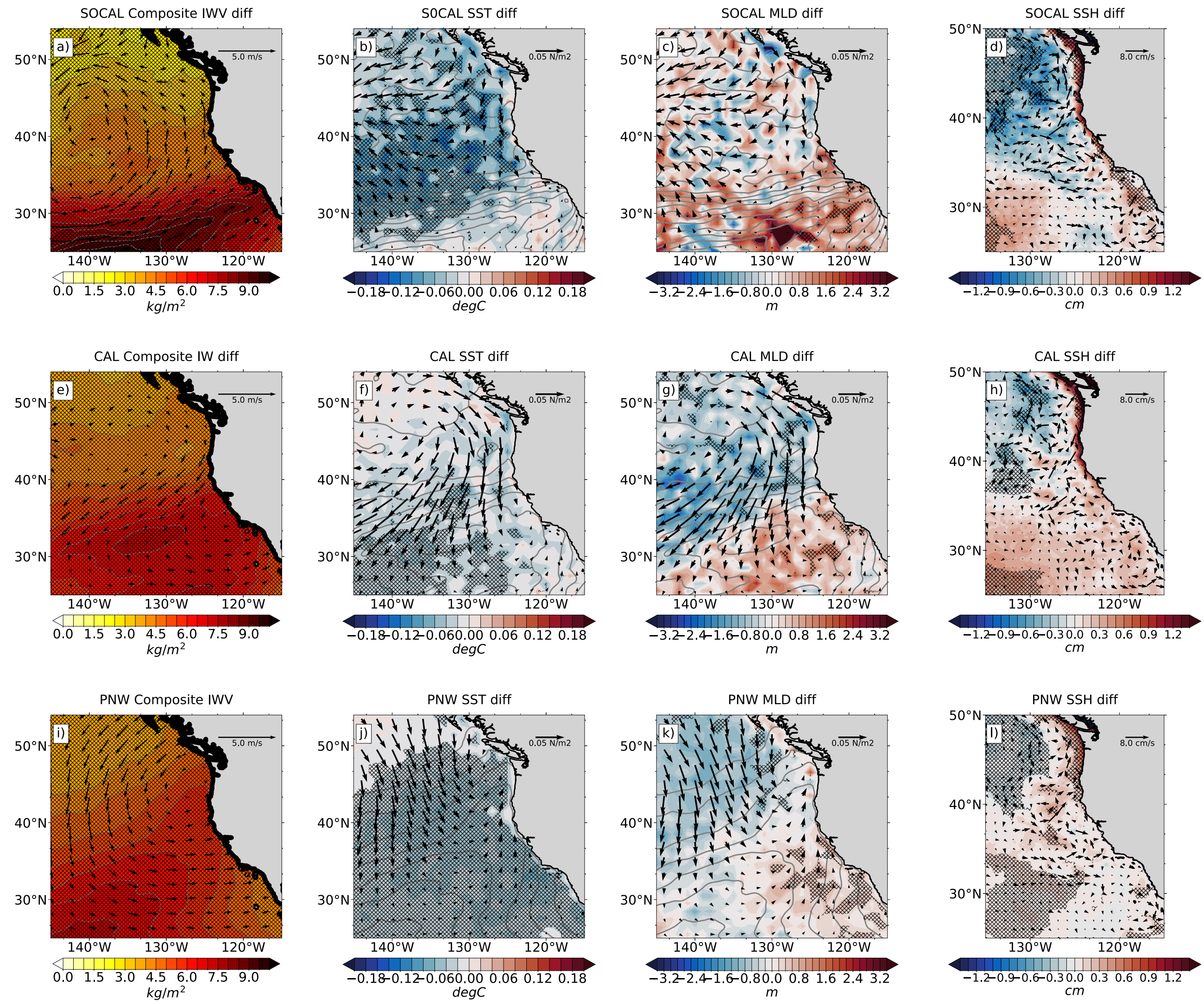

Fig. 4 | Climate change impact on sea surface temperature, mixed layer depth, and sea surface height. Future climate simulations minus the historical simulations for the same regions and variables similar to Fig. 2, i.e., SOCAL (**a**–**d**), CAL (**e**–**h**), and PNW (**i**–**l**). IWV (**a**, **f**, **k**, kgm^{-1}), SST (**b**, **g**, **l**, °C), MLD (**c**, **g**, **k**, cm), and SSH (**d**, **h**, **l**, cm). 850 hPa wind vectors (ms^{-1}) are overlaid on IWV in (**a**, **e**, **f**), and surface wind stress vectors (Nm^{-2}) are overlaid on SST and MLD. The panels (**d**, **h**, **l**) show the SSH and ocean surface current vectors (ms^{-1}) on the 0.1 degree model grid to show more details near the coastal region. Composites show ARDT consensus tracks. Anomalies are computed using 35-year long-term climatology using monthly means. IWV composite anomalies are shown as gray contours in each panel for location reference. Significance is shaded using *t*-test at 95%.

with ~14 W/m^2 heat entering the upper ocean well upstream of the AR landfalling impact sites (Table 1). Sensible heat is the dominant factor upstream for CAL ARs with stronger and more significant heating northwest of the ARs under climate change, although pockets of significance in latent heat are also important for parts of the domain. Increases in wind stress occur mostly for locations entering the convergence zone of the composite landfalling AR core which is suggestive of a shift equatorward of dominant winds (Figs. 2f and 4e). An enhanced heat flux entering the ocean is also found over the subtropical regions closer to the coast downstream of CAL landfalling ARs, which is likely attributable to reduced evaporation resulting from higher near-surface humidity (Supplemental Fig. 7). PNW ARs heat flux signals are generally weaker but consistent with CAL ARs with the overall effect of damping the fundamental AR passage signal seen in the historical simulations (Figs. 3 and 5), i.e., there is less cooling upstream the AR passage, again consistent with an overall warmer world. (For RCP8.5 responses, see Supplementary Figs. 8 and 9).

Heat and precipitation fluxes, in addition to wind stresses, shape the mixed layer climate change signal. From the historical simulation (Fig. 2), the mixed layer deepens to the northwest quadrant of the AR passage and shoals under the AR center. Under climate change, however, (Fig. 4c, g, k, and Supplementary Fig. 8) this “dipole-like” response persists, but the contrast is lessened, that is, a smaller reduction in MLD under the AR center, and a reduced deepening in mixed layer upstream the AR, but mostly for CAL (~1.23 m) and the PNW (~0.67 m). The weaker shoaling at the AR center may be attributed to changes in the ocean base state under global warming, with a warmer and shallower mixed layer in the AR region (Supplemental Fig. 5). This suggests that the heating under ARs may be less effective in modulating the MLD. Although results imply that the mixed layer gradient across the AR potentially becomes much weaker, consistent with overall warming, statistical significance (stippling) is not consistent across the entire domain but is generally limited to the strongest region of decreased shoaling (SOCAL and CAL). Under climate change, precipitation increases at the center of AR (Fig. 5d, h, l), which may moderate the influence from the heat fluxes on the mixed layer. The placement of the precipitation change is consistent with the notion that as the climate warms, AR landfall locations will also shift with the movement of the jets and storm tracks[71].

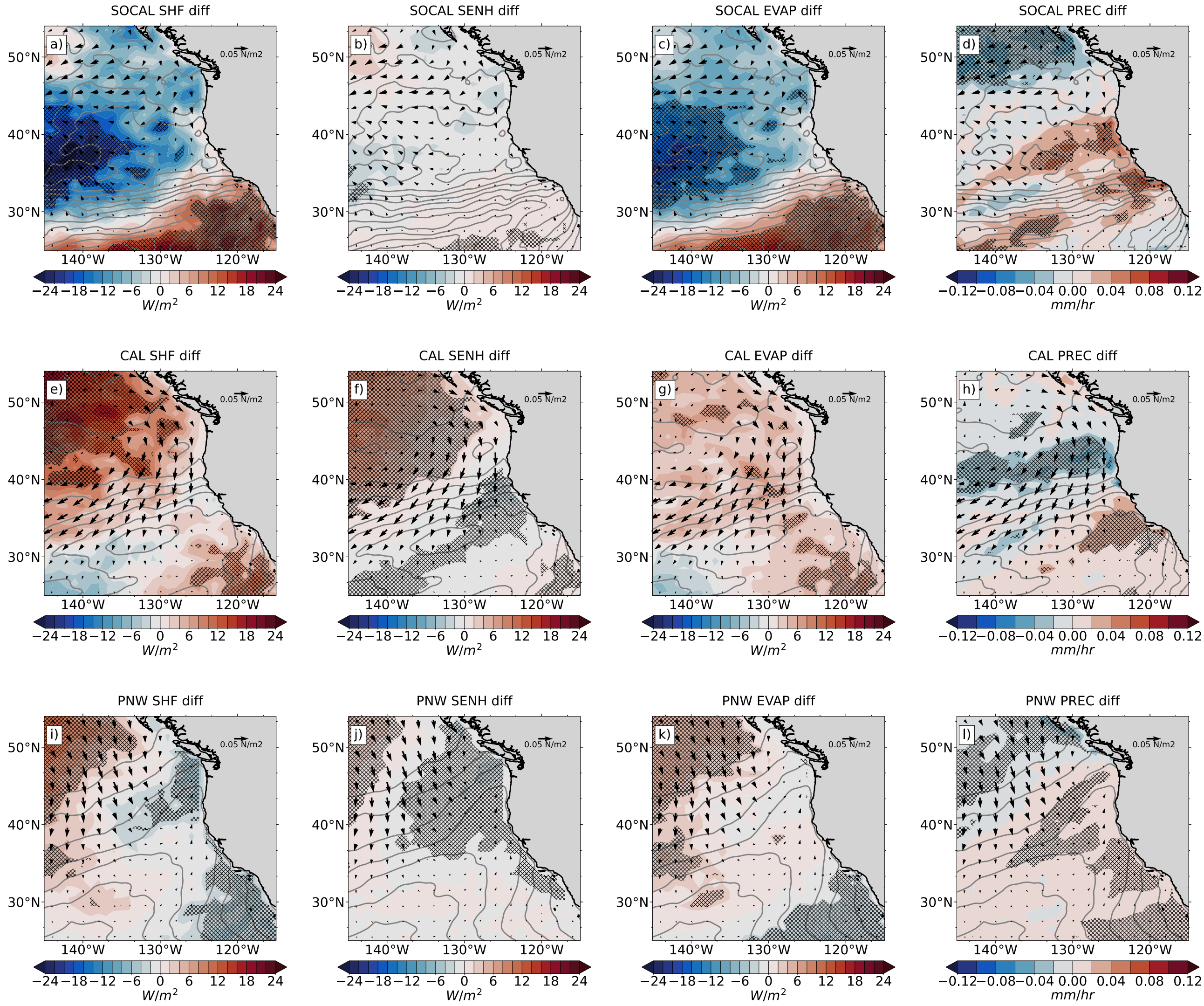

Fig. 5 | Climate change impact on ocean heat and precipitation fluxes. As in Fig. 4 but shows the corresponding changes in heat fluxes (Wm^{-2}) and precipitation (mmh^{-1}) for SOCAL (**a**–**d**), CAL (**e**–**h**) and PNW (**i**–**l**), specifically, SHF (**a**, **e**, **i**), SENF (**b**, **f**, **j**), EVAP (**c**, **g**, **k**), and PREC (**d**, **h**, **l**). Significance is shaded using *t*-test at 95%.

Table 1 | Area average of SST, MLD, SHF, and SSH at the AR upstream and downstream in the historical and RCP8.5 simulations

	SOCAL			CAL			PNW		
	HIST	RCP85	Diff	HIST	RCP85	Diff	HIST	RCP85	Diff
Upstream	35–50N, 130–155W			35–50N, 130–155W			40–55N, 135–160W		
Upstream SST	−0.22	−0.28	−0.08*	−0.29	−0.3	−0.04*	−0.27	−0.27	−0.03*
Upstream MLD	3.24	3.25	−1.03*	3.84	3.03	−1.23*	2.9	2.2	−0.67*
Upstream SHF	−41.26	−52.84	−20.36*	−43.41	−32.37	13.98*	−12.95	−3.75	10.65*
Downstream	20–30N, 120–130W			28–35N, 120–130W			30–40N, 125–135W		
Downstream SST	−0.03	−0.04	−0.04*	−0.04	−0.06	−0.04*	−0.08	−0.13	−0.04*
Downstream MLD	−1.0	0.42	2.74*	−0.09	0.61	1.3*	0.97	1.09	0.40*
Downstream SHF	25.6	41.67	17.24*	30.59	33.47	6.92*	13.38	12.67	−3.57*
Coastal SSH	0.14	0.48	0.63*	0.24	0.40	1.32*	0.13	0.20	0.26*

The upstream and downstream area for each region are defined based on the average AR location. The “Diff” column (numbers marked with *) shows the difference between the RCP8.5 and the historical simulation, in which case the area average is taken over the areas with 95% significance level, shown as the hatched area in Figs. 4 and 5. Units are m (MLD), °C (SST), Wm^{-2} (SHF), and cm (SSH).

While the wind stress responses vary across the different regions, the changes are generally small. However, the overall strong and prevailing westerly AR winds push the warmer water towards the coast, resulting in a significant and robust increase in SSH along the North American west coastline. In fact, under the projected warming, the coastal sea level rise caused by SOCAL and PNW ARs can exceed 200% (Supplemental Fig. 10).

Discussion and summary

ARs exert both dynamical and thermodynamic forcing onto the upper ocean. Using an eddy-resolving high horizontal resolution Earth System Model, we demonstrate the interaction between the North Pacific upper ocean and ARs impacting western North America, including their climate change signals. Applying eddy-resolving resolution to the ocean component of the coupled systems allows for more realistic structural characterization of ARs, and importantly, captures the ocean response with the enough fidelity to resolve the meso-synoptic scales. ARs act to push ocean water towards coastlines as measured by SSH, a forcing that will be exacerbated by climate change. Although consensus on AR climate change signals for metrics such as frequency, duration, and location of landfall along North American coastlines is still uncertain[16,18,19], stakeholders in coastal communities still need to plan for all possible scenarios. Questions of when, where, and how often will ARs reach their shores need to be answered. In addition to the typical impacts such as precipitation extremes, coastal erosion, and flooding must be considered, especially with a potential for higher sea levels during storms.

Mixed layers are generally deeper (shallower) upstream (downstream) of AR passages, although under climate change, this fundamental response potentially changes with less shoaling downstream of the AR. Wind forcing and the associated heat fluxes promote cooling (warming) upstream (downstream) the AR passage. The impact of climate change on the sign and character of the heat flux response is largely region dependent. Evaporative cooling dominates the heat flux climate change signal upstream of SOCAL ARs, while their more northern counterparts are composed of both latent and sensible heat warming contributions. Our study finds that AR forcing on upper ocean heat fluxes is strengthened under climate change for SOCAL because the total SHF response is driven by the evaporative processes that account for the increase in wind stress and moisture. For CAL and PNW ARs, the heat flux response is subdued, and sensible heat plays a larger role in the total change. Table 1 summarizes all these results quantitatively, both upstream and downstream of the AR.

The analysis presented here is a first-order exploration of the different dynamical and thermodynamic mechanisms for basic upper ocean processes in response to ARs, i.e., SSH for horizontal displacement, MLD for turbulent mixing, sensible and evaporative heating for energy in and out of the upper ocean. However, this is not an exhaustive list, and further analysis is needed to better understand the interactions between AR wind, precipitation, ocean turbulent mixing, and MLD. For example, analyzing subsurface ocean stratification and ocean heat budget is necessary to further validate the mechanisms driving ocean temperature and mixed layer changes and attribute the effect of AR winds versus precipitation. However, saving the full-depth eddy-resolving ocean output at daily frequency poses a computational challenge and is not available for the current study. Additionally, although the heat fluxes responses can be broadly explained by sensible versus latent heat components, other factors may also be at work, such as the different types or "flavors" of storms that are part of the larger AR synoptic system. ARs are almost always associated with an extratropical cyclone for PNW storms and are often included in CAL storms. Less so for SOCAL which is dominated by the "Pineapple Express" variety of moisture transport which runs along stationary fronts or simple surface temperature gradients. The differences in surface wind stresses under climate change across these regions hint that different types of synoptic storms are important for different regions. This follows for other regions of the world, for example, North Atlantic ARs may have very different heat flux responses compared to the North Pacific because North Atlantic ARs that impact European coastlines almost always lie within the storm track and include strong extratropical cyclones that incorporate both moisture transport (AR) and warm conveyor belt dynamics[72]. Other processes such as cloud and aerosol forcing are wide and varied for different AR-occurring regions around the world and would likely impact local thermodynamic responses as well. Finally, as with any climate change study, projections should be tempered in the context of model uncertainty. In the climate model community, when allocating project resources, a tension exists between the need for applying cutting-edge, high-fidelity simulations, and the use of multiple model frameworks (i.e., lower resolution Coupled Model Intercomparison Project (CMIP)), or additional ensemble members within the same model framework. For this study, the need for an eddy-resolving ocean, and a high-resolution atmosphere, both capable of more accurately characterizing AR impacts, directed this choice. We address uncertainty in projections by applying a small ensemble of simulations with three unique ways of defining ARs, which is arguably the greater source of AR uncertainty than using multiple models, or larger ensembles[18]. This study clearly demonstrates that high-resolution Earth System Models can accurately simulate the AR-ocean relationship first explored with observations by Shinoda et al.[43]. Further, under climate change, two key points can be made: (1) dynamical changes are consistent across North American regions, i.e., coastal communities can largely expect increased impacts due to displaced seas pushed towards their shores, and (2) thermodynamic changes are regionally dependent and require further study.

Table 2 | Available simulations from the high resolutions CESM1.3 project[59,81]

Simulation	Years for AR analysis	Ensemble members
Historical "BHIST"	1960–2005	002, 003
RCP8.5 "BRCP85"	2060–2100	002, 003

001 was not used because it did not have the necessary output data for AR tracking.

Methods

High-resolution Community Earth System Model (CESM)

Description of model. A detailed description of the high-resolution version of CESM (CESM-HR) can be found in ref. 59 Here we only give a brief overview of the model. CESM-HR is based on an earlier version of CESM1.3 described by Meehl et al.[63] with many additional modifications and improvements. The CESM-HR component models are the Community Atmosphere Model version 5[73] with the Spectral Element dynamical core, the Parallel Ocean Program version 2[74,75], the Community Ice Code version 4[76], and the Community Land Model version 4[77]. CESM-HR uses a horizontal resolution of 0.25° (~25 km) for the atmosphere and land models, and nominal 0.1° (~10 km at the Equator down to ~4 km at high latitudes) for the ocean and sea-ice models.

Description of simulations. The first step toward building the 3-member ensemble of CESM-HR transient climate simulations (Table 2) used in this study is a multi-century 500-year preindustrial control (PI-CTRL) simulation (Supplementary Fig. 11). The PI-CTRL is forced by a perpetual climate forcing that corresponds to the year 1850 conditions. The first member is then branched from PI-CTRL at year 250 and it is integrated forward from year 1850 to 2100 (Supplementary Fig. 11). Ensembles 002 and 003 are subsequently started from the year 1920 of ensemble 001 and integrated forward to 2100 (Supplementary Fig. 11). Spread in the ensemble is generated by applying round-off level perturbations in the January 1st of 1920 air temperature fields used to initialize member 2 and 3. All 3 members use the same specified external forcing. Following the protocol for the Coupled Model Intercomparison Project phase 5 (CMIP5) experiments, historical forcing is used from 1920 to 2005[78] followed by the RCP8.5 forcing[79] from 2006 to 2100.

All 3 members produce a warming of ~4.5 °C in response to the applied historical and RCP8.5 external forcing from 1920 to 2100 (Supplementary Fig. 11). The warming produced by CESM-HR is consistent with the

Table 3 | ARDT Overview includes developer, ARDT characterization, a brief descriptive overview, and the DOI citation(s) that provide full and complete algorithmic details

Developer	ARDT characterization	Description overview	Citation DOI
Shields/Kiehl	Threshold based, very restrictive	Time varying and spatially relative; anomalies are computed for moisture threshold using IWV; Wind threshold defined by regional 85th percentile 850 mb wind magnitudes; geometric requirements	https://doi.org/10.1002/2016GL069476 https://doi.org/10.1002/2016GL070470
Mundhenk/Nardi	Threshold based, less restrictive	Fixed relative based on reference climatology from historical period; IVT percentiles and/or anomalies both temporal and spatial; geometric requirements	https://doi.org/10.1175/JCLI-D-15-0655.1 https://doi.org/10.1175/MWR-D-18-0060.1 https://doi.org/10.1029/2021JD036013
IPART	Threshold-free, moderately restrictive	Image recognition, select transient IVT plumes standing out from a temporal scale of 8 days; Spatial scale of ~1000 km	https://doi.org/10.5194/gmd-13-4639-2020 https://doi.org/10.1029/2022MS003081

To provide context, Supplementary Fig. 2 plots the three ARDTs applied to this work along with all ARTMIP ARDTs.

warming from the standard resolution version of the model[59]. The rate of warming simulated by CESM-HR over the observational period agrees very well with the observed rate of warming derived from the Goddard Institute for Space Studies Surface Temperature Analysis[80] (Supplementary Fig. 11). Further validation of the CESM-HR 3-member ensemble is provided in Chang et al.[81] and Supplementary Fig. 12. Chang et al.[81] focuses on the Eastern Boundary Upwelling System (EBUS). EBUS are poorly represented in the current generation of climate models with systematic warm biases of up to 4 °C in simulated sea-surface temperature[82]. Evident improvements are found in CESM-HR[81]. The improvements are associated with more realistic low-level coastal wind jets, as well as the ability to explicitly resolve ocean mesoscale eddies and fronts. As a result, the CESM-HR simulated SSTs in EBUS show remarkable agreement with the observations, and a much reduced bias, including in the CAL Current System along the US West Coast, the region of interest for the present study. Unfortunately, the high-frequency outputs needed for the AR tracking are not available from ensemble member 1. As a result, the analysis presented in this manuscript will focus solely on members 2 and 3. However, between the two ensemble members used for AR tracks, in combination with three distinct ARDTs (Atmospheric River Detection Tools, (next section), ample AR statistics are produced to provide a robust characterization of AR impacts onto the upper ocean.

AR detection tools

The definition of an AR has been a source of debate in the AR community since the term was first coined a quarter century ago[1,68]. The Atmospheric River Tracking Method Intercomparison Project (ARTMIP)[11,12] was born out of the need to not only quantify uncertainties in AR metrics across different methodologies, but to understand the purpose of each unique tool. Each ARDT is designed to address specific science questions that range from the physics to the impacts of ARs. For example, impact-driven AR research tends to favor less restrictive algorithms because ultimately the stakeholder cares more about how much flooding will occur, for example, rather than the physical structure of the weather phenomena itself. However, given the research community uses the same metrics to characterize ARs across different studies, (frequency, duration, and intensity), despite fundamental differences in what is being detected, it has become necessary to provide context for individual ARDTs compared to each other, and to quantify the spread of possibilities for metrics tied to AR definition, such as frequency. The below section and Table 3 summarize three separate ARDTs, all developed for similar purposes, but each applying very different methodologies and developed independently. The ARDTs were chosen to represent different levels of restrictiveness and thresholding philosophies to realistically represent spread and uncertainty in AR characterization. Only landfalling ARs are considered, but full synoptics for each individual AR are used in composites. The mean latitude of landfall is used for each AR which adopts the Shields and Kiehl ARDT convention for consistency. For example, the AR in Fig. 1a would be included in the PNW region.

Shields/Kiehl. The Shields/Kiehl (SK)[61,71] is designed to identify the strongest ARs making landfall over Western North America with high-resolution gridded data. It is one of the most restrictive ARTMIP ARDTs and uses time-varying relative methodology and computes thresholds based on spatial anomalies of IWV and 850 hPa wind. ARs must make landfall with a southwestern origin and minimum wind values of the 85th percentile and require a length:width ratio of 2:1. The SK ARDT detects landfall latitudes and does not provide a spatial footprint which is a limitation when directly compared to other methods, however, the philosophy behind this method is to identify latitude of landfall for each time step, then return to the source data for the full synoptic signature for each respective analysis. Other ARDTs were conformed to the SK latitude of landfall per time step metric for comparison.

Mundhenk/Nardi. The global Mundhenk/Nardi algorithm is an updated version of the regional algorithm first described in ref. 83. Originally designed to analyze the climatology and variability of ARs over the North Pacific Ocean, the algorithm was later updated to be applied globally using a fixed IVT anomaly threshold based on a given dataset's IVT climatology[18]. The Mundhenk/Nardi algorithm has been applied for various applications, including historical AR variability[83], operational predictability of ARs[84,85], and the depiction of ARs in climate models[18]. At each grid cell in the input dataset, the time series of IVT is calculated, and a smoothed seasonal cycle is removed to produce a time series of IVT anomalies at each grid cell. To detect candidate AR objects at a given time and location, the algorithm looks for grid cells that exceed a static IVT anomaly threshold, which is equal to the 94th percentile of all IVT anomalies over the entirety of the temporal and spatial domain, within each dataset. To remain consistent with prior applications of the Mundhenk/Nardi algorithm[18], the anomaly threshold is calculated over the North Pacific only. Clusters of connected grid cells where the IVT anomaly exceeds the threshold are labeled as unique AR candidate objects. Each candidate object is subsequently put through various geometrics tests, including for length (>1400 km), area (>300,000 km^2), and aspect ratio (>1.4), to isolate long, narrow plumes of enhanced water vapor transport. While it includes tests to remove rotating low-latitude features, the algorithm occasionally detects tropical cyclones as ARs, although these features rarely manifest in the midlatitudes.

IPART. Unlike methods that heavily rely on magnitude thresholds, IPART stands out as an image-processing-based tracking method that operates independently of magnitudes[86]. In this study, we applied IPART on the IVT field by initially filtering the spatiotemporal spikiness of the image to determine the AR candidates. Then, geometrical filtering, incorporating criteria such as minimum/maximum length and area, length/width ratio, and latitude range, was applied to eliminate non-AR systems such as tropical cycles[86]. Conventional AR tracking methods are sensitive to the intensity of AR-related vapor fluxes. They require different threshold values for different regions such as midlatitude and polar systems. IPART avoids this issue by applying the filtering process to obtain the filamentary fields. It demonstrates reduced sensitivity to parameters and enhanced reliability in detecting ARs globally within a warm climate or across various models with inherent biases. Nevertheless, IPART still exhibits sensitivities in other aspects, particularly in the interaction between candidate AR region detection and subsequent geometrical filtering. The ambiguity in AR shape remains a significant source of uncertainty in this AR tracking method.

AR analysis procedures

Analysis locations can be subdivided into regions based on AR characteristics with unique climatologies[71[,87]. Here we define regional areas as SOCAL (32°–35°N), CAL (35°–41°N), and PNW (41°–52°N), (Fig. 1a). Detection is completed using 6-hourly instantaneous model output for each respective ARDT. Variable composites are computed using all landfalling instances. Composite anomalies are computed by subtracting the long-term 20 year monthly mean climatology from the variable. Monthly mean is applied to avoid seasonal cycle signatures. SST and MLD AR fingerprint is determined by using composite anomalies 3 days after AR onset minus 3 days before AR passage, however SSH uses the convention of 1 after onset day minus 3 days before passage to maximize the SSH fingerprint. Heat flux anomaly composites incorporate the 3-day average (one day before and after AR passage). Only consensus AR landfalls are used in composites. Consensus is defined as all three ARDTs in agreement for each landfall occurrence. Ocean flux conventions are positive down into the ocean (i.e., a positive heat flux warms the ocean).

Reporting summary

Further information on research design is available in the Nature Portfolio Reporting Summary linked to this article.

Data availability

All data associated with this work is published at NSF NCAR's Research Data Archival facility https://doi.org/10.5065/RFWZ-VM18. This includes ARDT catalogs, source tracking data, and model output data used for analysis and plots.

Code availability

High-resolution CESM1.3 code is found on github: https://github.com/ihesp/cesm/tree/cesm-ihesp-hires1.0.46.

Received: 25 April 2024; Accepted: 10 October 2024;

References

1. Zhu, Y. & Newell, R. E. A proposed algorithm for moisture fluxes from atmospheric rivers. *Mon. Weather Rev.* **126**, 725–735 (1998).
2. Neiman, P. J., Ralph, F. M., Wick, G. A., Lundquist, J. D. & Dettinger, M. D. Meteorological characteristics and overland precipitation impacts of atmospheric rivers affecting the West Coast of North America based on eight years of SSM/I satellite observations. *J. Hydrometeol.* **9**, 22–47 (2008).
3. Ralph, F. M., Neiman, P. J. & Wick, G. A. Satellite and CALJET aircraft observations of atmospheric rivers over the eastern North-Pacific Ocean during the El Niño winter of 1997/98. *Mon. Weather Rev.* **132**, 1721–1745 (2004).
4. Lavers, D. A. & Villarini, G. The nexus between atmospheric rivers and extreme precipitation across Europe. *Geophys. Res. Lett.* **40**, 3259–3264 (2013).
5. Payne, A. E. & Magnusdottir, G. Persistent landfalling atmospheric rivers over the west coast of North America. *J. Geophys. Res. Atmos.* **121**, 13,287–13,300 (2016).
6. Guan, B. & Waliser, D. E. Atmospheric rivers in 20 year weather and climate simulations: a multimodel, global evaluation. *J. Geophys. Res. Atmos.* **122**, 5556–5581 (2017).
7. Goldenson, N., Leung, L. R., Bitz, C. M. & Blanchard-Wrigglesworth, E. Influence of atmospheric rivers on mountain snowpack in the Western United States. *J. Clim.* **31**, 9921–9940 (2018).
8. Young, A. M., Skelly, K. T. & Cordeira, J. M. High-impact hydrologic events and atmospheric rivers in California: an investigation using the NCEI Storm Events Database. *Geophys. Res. Lett.* **44**, 3393–3401 (2017).
9. Albano, C. M., Dettinger, M. D. & Soulard, C. E. Influence of atmospheric rivers on vegetation productivity and fire patterns in the southwestern U.S. *J. Geophys. Res. Biogeosci.* **122**, 308–323 (2017).
10. Chen, X., Leung, L. R., Wigmosta, M. & Richmond, M. Impact of atmospheric rivers on surface hydrological processes in western U.S. watersheds. *J. Geophys. Res. Atmos.* **124**, 8896–8916 (2019).
11. Shields, C. A. et al. Atmospheric River Tracking Method Intercomparison Project (ARTMIP): project goals and experimental design. *Geosci. Model Dev.* **11**, 2455–2474 (2018).
12. Rutz, J. J. et al. The Atmospheric River Tracking Method Intercomparison Project (ARTMIP): quantifying uncertainties in atmospheric river climatology. *J. Geophys. Res. Atmos.* **124**, 13777–13802 https://doi.org/10.1029/2019JD030936. (2019)
13. Collow, A. B. et al. An overview of ARTMIP's tier 2 reanalysis intercomparison: uncertainty in the detection of atmospheric rivers and their associated precipitation. *J. Geophys. Res. Atmos.* **127**, e2021JD036155 (2022).
14. Lavers, D. A., Ralph, F. M., Waliser, D. E., Gershunov, A. & Dettinger, M. D. Climate change intensification of horizontal water vapor transport in CMIP5. *Geophys. Res. Lett.* **42**, 5617–5625 (2015).
15. Espinoza, V., Waliser, D. E., Guan, B., Lavers, D. A. & Ralph, F. M. Global analysis of climate change projection effects on atmospheric rivers. *Geophys. Res. Lett.* **45**, 4299–4308 (2018).
16. Payne, A. E. et al. Responses and impacts of atmospheric rivers to climate change. *Nat. Rev. Earth Environ.* **1**, 143–157 (2020).
17. Rhoades, A. M. et al. The shifting scales of western U.S. landfalling atmospheric rivers under climate change. *Geophys. Res. Lett.* **47**, e2020GL089096 (2020).
18. O'Brien, T. A. et al. Increases in future AR count and size: overview of the ARTMIP tier 2 CMIP5/6 experiment. *J. Geophys. Res. Atmos.* **127**, e2021JD036013 (2022).
19. Shields, C. A. et al. Future atmospheric rivers and impacts on precipitation: overview of the ARTMIP Tier 2 high-resolution global warming experiment. *Geophys. Res. Lett.* **50**, e2022GL102091 (2023).
20. Dettinger, M. D. Atmospheric rivers as drought busters on the US West Coast. *J. Hydrometeorol.* **14**, 1721–1732 (2013).
21. Lavers, D. A. & Villarini, G. The contribution of atmospheric rivers to precipitation in Europe and the United States. *J. Hydrol.* **522**, 382–390 (2015).
22. DeFlorio, M. J. et al. From California's extreme drought to major flooding: evaluating and synthesizing experimental seasonal and subseasonal forecasts of landfalling atmospheric rivers and extreme precipitation during winter 2022/23. *Bull. Amer. Meteor. Soc.* **105**, E84–E104 (2024).
23. Blamey, R. C., Ramos, A. M., Trigo, R. M., Tomé, R. & Reason, C. J. C. The influence of atmospheric rivers over the South Atlantic on winter rainfall in South Africa. *J. Hydrometeorol.* **19**, 127–142 (2018).
24. Viale, M., Valenzuela, R., Garreaud, R. D. & Ralph, F. M. Impacts of atmospheric rivers on precipitation in Southern South America. *J. Hydrometeorol.* **19**, 1671–1687 (2018).
25. Reid, K. J., King, A. D., Lane, T. P. & Short, E. The sensitivity of atmospheric river identification to integrated water vapor transport

threshold, resolution, and regridding method. *J. Geophys. Res. Atmos.* **125**, e2020JD032897 (2020).
26. Reid, K. J., Rosier, S. M., Harrington, L. J., King, A. D. & Lane, T. P. Extreme rainfall in New Zealand and its association with atmospheric rivers. *Environ. Res. Lett.* **16**, 044012 (2021).
27. Esfandiari, N. & Shakiba, A. The extraordinary atmospheric rivers analysis over the Middle East: large-scale drivers, structure, effective sources, and precipitation characterization. *Dyn. Atmos. Oceans* **105**, 101430 (2024).
28. Park, C., Son, S.-W. & Kim, H. Distinct features of atmospheric rivers in the early versus late east Asian summer monsoon and their impacts on monsoon rainfall. *J. Geophys. Res. Atmos.* **126**, e2020JD033537 (2021).
29. Francis, D., Mattingly, K. S., Temimi, M., Massom, R. & Heil, P. On the crucial role of atmospheric rivers in the two major Weddell Polynya events in 1973 and 2017 in Antarctica. *Sci. Adv.* **6**, eabc2695 (2020).
30. Zhang, P. et al. More frequent atmospheric rivers slow the seasonal recovery of Arctic sea ice. *Nat. Clim. Chang.* **13**, 266–273 (2023).
31. Li, L. et al. Impact of atmospheric rivers on Arctic sea ice variations. *Cryosphere* **18**, 121–137 (2024).
32. Gorodetskaya, I. V. et al. The role of atmospheric rivers in anomalous snow accumulation in East Antarctica. *Geophys. Res. Lett.* **41**, 6199–6206 (2014).
33. Wille, J. D. et al. Intense atmospheric rivers can weaken ice shelf stability at the Antarctic Peninsula. *Commun. Earth Environ.* **3**, 90 (2022).
34. Maclennan, M. L. et al. Climatology and surface impacts of atmospheric rivers on West Antarctica. *Cryosphere* **17**, 865–881 (2023).
35. Mattingly, K. S. et al. Increasing extreme melt in northeast Greenland linked to foehn winds and atmospheric rivers. *Nat. Commun.* **14**, 1743 (2023).
36. Baiman, R. et al. Synoptic and planetary-scale dynamics modulate antarctic atmospheric river precipitation intensity. *Commun. Earth Environ.* **5**, 127 (2024).
37. Kamae, Y., Mei, W. & Xie, S. P. Ocean warming pattern effects on future changes in East Asian atmospheric rivers. *Environ. Res. Lett.* **14**, 054019 (2019).
38. McClenny, E. E., Ullrich, P. A. & Grotjahn, R. Sensitivity of atmospheric river vapor transport and precipitation to uniform sea surface temperature increases. *J. Geophys.Res. Atmos.* **125**, e2020JD033421 (2020).
39. Chen, X. & Leung, L. R. Response of landfalling atmospheric rivers on the U.S. west coast to local sea surface temperature perturbations. *Geophys. Res. Lett.* **47**, e2020GL089254 (2020).
40. Liu, X. et al. Ocean fronts and eddies force atmospheric rivers and heavy precipitation in western North America. *Nat. Commun.* **12**, 1268 (2021).
41. Bartusek, S. T., Seo, H., Ummenhofer, C. C. & Steffen, J. The role of nearshore air-sea interactions for landfalling atmospheric rivers on the U.S. West Coast. *Geophys. Res. Lett.* **48**, e2020GL091388 (2021).
42. Sun, R. et al. The role of air-sea interactions in atmospheric rivers: case studies using the SKRIPS regional coupled model. *J. Geophys. Res. Atmos.* **126**, e2020JD032885 (2021).
43. Shinoda, T. et al. Ocean variability and air-sea fluxes produced by atmospheric rivers. *Sci. Rep.* **9**, 2152 (2019).
44. Gottschalck, J., Roundy, P. E., Schreck III, C. J., Vintzileos, A. & Zhang, C. Large-scale atmospheric and oceanic conditions during the 2011–12 DYNAMO field campaign. *Mon. Wea. Rev.* **141**, 4173–4196 (2013).
45. Guan, B., Lee, T., Halkides, D. J. & Waliser, D. E. Aquarius surface salinity and the Madden-Julian Oscillation: the role of salinity in surface layer density and potential energy. *Geophys. Res. Lett.* **41**, 2858–2869 (2014).
46. Riser, S. C., Yang, J. & Drucker, R. Observations of large-scale rainfall, wind, and sea surface salinity variability in the eastern tropical Pacific. *Oceanography* **32**, 42–49 (2019).
47. Lindstrom, E. J., Edson, J. B., Schanze, J. J. & Shcherbina, A. Y. SPURS-2: Salinity processes in the upper-ocean regional study 2. The eastern equatorial Pacific experiment. *Oceanography* **32**, 15–19 (2019).
48. Iyer, S. & Drushka, K. Turbulence within rain-formed fresh lenses during the SPURS-2 experiment. *J. Phys. Oceanogr.* **51**, 1705–1721 (2021).
49. Han, C., Bowen, M. & Sutton, P. The response of the upper ocean to tropical cyclones in the South Pacific. *J. Geophys. Res. Oceans* **129**, e2023JC020627 (2024).
50. Zhang, H. et al. Upper ocean response to tropical cyclones: a review. *Geosci. Lett.* **8**, 1 (2021).
51. Karnauskas, K. B., Zhang, L. & Emanuel, K. A. The feedback of cold wakes on tropical cyclones. *Geophys. Res. Lett.* **48**, e2020GL091676 (2021).
52. Pasquero, C., Desbiolles, F. & Meroni, A. N. Air-sea interactions in the cold wakes of tropical cyclones. *Geophys. Res. Lett.* **48**, e2020GL091185 (2021).
53. Phillips, B. & O'Neill, L. Observational analysis of extratropical cyclone interactions with Northeast Pacific Sea surface temperature anomalies. *J. Clim.* **33**, 6745–6763 (2020).
54. Yao, Y., Perrie, W., Zhang, W. & Jiang, J. Characteristics of atmosphere-ocean interactions along North Atlantic extratropical storm tracks. *J. Geophys. Res.* **113**, D14124 (2008).
55. Price, J. F. Upper Ocean response to a hurricane. *J. Phys. Oceanogr.* **11**, 153–175 (1981).
56. Liu, J., Curry, J. A., Clayson, C. A. & Bourassa, M. A. High-resolution satellite surface latent heat fluxes in North Atlantic hurricanes. *Mon. Wea. Rev.* **139**, 2735–2747 (2011).
57. Domingues, R. et al. Ocean observations in support of studies and forecasts of tropical and extratropical cyclones. *Front. Marine Sci.* **6**, 446 (2019).
58. Liu, X. et al. Improved simulations of atmospheric river climatology and variability in high-resolution CESM. *J. Adv. Model. Earth Syst.* **14**, e2022MS003081 (2022).
59. Chang, P. et al. An unprecedented set of high-resolution earth system simulations for understanding multiscale interactions in climate variability and change. *J. Adv. Model. Earth Syst.* **12**, e2020MS002298 (2020).
60. Wang, Z. et al. The Northern Hemisphere wintertime storm track simulated in the high-resolution Community Earth System Model. *J. Adv. Model. Earth Syst.* **15**, e2023MS003652 (2023).
61. Shields, C. A. & Kiehl, J. T. Simulating the pineapple express in the half degree community climate system model, CCSM4. *Geophys. Res. Lett.* **43**, 7767–7773 (2016).
62. Demory, M.-E. et al. European daily precipitation according to EURO-CORDEX regional climate models (RCMs) and high-resolution global climate models (GCMs) from the High-Resolution Model Intercomparison Project (HighResMIP). *Geosci. Model Dev.* **13**, 5485–5506 (2020).
63. Meehl, G. A. et al. Effects of model resolution, physics, and coupling on Southern Hemisphere storm tracks in CESM1.3. *Geophys. Res. Lett.* **46**, https://doi.org/10.1029/2019GL084057 (2020).
64. Dagon, K. et al. Machine learning-based detection of weather fronts and associated extreme precipitation in historical and future climates. *J. Geophys. Res. Atmos.* **127**, e2022JD037038 (2022).
65. Small, R. J. et al. A new synoptic scale resolving global climate simulation using the community earth system model. *J. Adv. Model. Earth Syst.* **6**, 1065–1094 (2014).
66. Large, W., Danabasoglu, G., Doney, S. & McWilliams, J. Sensitivity to surface forcing and boundary layer mixing in the NCAR CSM ocean

model: annual-mean climatology. *J. Phys. Oceanogr.* **27**, 2418–2447 (1997).
67. American Meteorological Society, 2017: Atmospheric river. *Glossary of Meteorology*, http://glossary.ametsoc.org/wiki/Atmospheric_river.
68. Ralph, F. M., Dettinger, M. D., Cairns, M. M., Galarneau, T. J. & Eylander, J. Defining “atmospheric river”: how the Glossary of Meteorology helped resolve a debate. *Bull. Am. Meteorol. Soc.* **99**, 837–839 (2018).
69. Guo, Y., Shinoda, T., Guan, B., Waliser, D. E. & Chang, E. K. M. Statistical relationship between atmospheric rivers and extratropical cyclones and anticyclones. *J. Clim.* **33**, 7817–7834 (2020).
70. Gimeno, L., Algarra, I., Eiras-Barca, J., Ramos, A. M., & Nieto, R. Atmospheric river, a term encompassing different meteorological patterns. *Wiley Interdiscip. Rev. Water*, **8**, e1558 (2021).
71. Shields, C. A. & Kiehl, J. T. Atmospheric river landfall-latitude changes in future climate simulations. *Geophys. Res. Lett.* **43**, 8775–8782 (2016).
72. Dacre, H. F., Martínez-Alvarado, O. & Mbengue, C. O. Linking atmospheric rivers and warm conveyor belt airflows. *J. Hydrometeor.* **20**, 1183–1196 (2019).
73. Neale, R. B. et al. Description of the NCAR community atmosphere model (CAM 5.0). *NCAR Tech. Note NCAR/TN-486+ STR* **1**, 1–12 (2010).
74. Danabasoglu, G. et al. The community Earth system model version 2 (CESM2). *J. Adv. Mod. Earth Syst.* **12**, e2019MS001916 (2020).
75. Smith, R. et al. The Parallel Ocean Program (POP) reference manual: Ocean component of the Community Climate System Model (CCSM), *LAUR-01853*, **141**, 1–140 https://opensky.ucar.edu/islandora/object/manuscripts%3A825 (Original work published, 2010).
76. Hunke, E., Lipscomb, W., Jones, P., Turner, A., Jeffery, N., & Elliott, S. CICE, The Los Alamos Sea Ice Model (Version 00) [Computer software]. https://www.osti.gov//servlets/purl/1364126 (2017).
77. Lawrence, D. M. et al. The Community Land Model Version 5: description of new features, benchmarking, and impact of forcing uncertainty. *J. Adv. Model. Earth Syst.* **11**, 4245–4287 (2019).
78. Lamarque, J. F. et al. Historical (1850–2000) gridded anthropogenic and biomass burning emissions of reactive gases and aerosols: methodology and application. *Atmos. Chem. Phys.* **10**, 7017–7039 (2010).
79. Lamarque, J. F. et al. Global and regional evolution of short-lived radiatively-active gases and aerosols in the Representative Concentration Pathways. *Clim. Chang.* **109**, 191 (2011).
80. Hansen, J., Ruedy, R., Sato, M. & Lo, K. Global surface temperature change. *Rev. Geophys.* **48**, RG4004 (2010).
81. Chang, P. et al. Uncertain future of sustainable fisheries environment in eastern boundary upwelling zones under climate change. *Commun. Earth Environ.* **4**, 19 (2023).
82. Ma, H. et al. On the correspondence between seasonal forecast biases and long-term climate biases in sea surface temperature. *J. Clim.* **34**, 427–446 (2021).
83. Mundhenk, B., Barnes, E. & Maloney, E. All-season climatology and variability of atmospheric river frequencies over the North Pacific. *J. Clim.* **29**, 4885–4903 (2016).
84. Mundhenk, B., Barnes, E., Maloney, E. & Nardi, K. Modulation of atmospheric rivers near Alaska and the U.S. West Coast by Northeast Pacific height anomalies. *J. Geophys. Res.* **121**, 12751–12765 (2016).
85. Nardi, K., Barnes, E. & Ralph, F. M. Assessment of numerical weather prediction model reforecasts of the occurrence, intensity, and location of atmospheric rivers along the West Coast of North America. *Mon. Wea. Rev.* **146**, 3343–3362 (2018).
86. Xu, G., Ma, X., Chang, P. & Wang, L. Image-processing-based atmospheric river tracking method version 1 (IPART-1). *Geosci. Model Dev.* **13**, 4639–4662 (2020).
87. Gonzales, K. R., Swain, D. L., Nardi, K. M., Barnes, E. A. & Diffenbaugh, N. S. Recent warming of landfalling atmospheric rivers along the west coast of the United States. *J. Geophys. Res. Atmos.* **124**, 6810–6826 (2019).

Acknowledgements

Portions of this study were supported by the Regional and Global Model Analysis (RGMA) component of the Earth and Environmental System Modeling Program of the U.S. Department of Energy’s Office of Biological & Environmental Research (BER) under Award Number DE-SC0022070. This work also was supported by the National Center for Atmospheric Research, which is a major facility sponsored by the National Science Foundation (NSF) under Cooperative Agreement No. 1852977. The initial simulations were completed through the International Laboratory for High Resolution Earth System Prediction (iHESP) project, a collaboration between the Qingdao National Laboratory for Marine Science and Technology (QNLM), Texas A&M University (TAMU), and the U.S. National Science Foundation National Center for Atmospheric Research (NSF NCAR). The CESM-HR effort is now supported by the NSF Division of Atmospheric and Geospace Sciences (AGS) Climate & Large-Scale Dynamics program under Grant #2231237. NSF NCAR is a major facility sponsored by the NSF under Cooperative Agreement 1852977. We acknowledge the Texas Advanced Computing Center (TACC) for providing HPC resources on Frontera, where many centuries of CESM-HR were integrated. We also acknowledge high-performance computing support from Derecho: HPE Cray EX System provided by NSF NCAR’s Computational and Information Systems Laboratory (CISL) where most of the analyses were carried out. CMZ was supported by the U.S. Department of Energy, Office of Science, Office of Biological and Environmental Research program under Award DE-SC0016605 “A framework for improving analysis and modeling of Earth system and intersectoral dynamics at regional scales.” Finally, we would like to thank the editor and anonymous reviewers for their helpful feedback.

Author contributions

C.A. Shields contributions include project management, research design, majority writing, analysis, AR tracking, and Fig. 1 and Supplementary Figs. 1, 13 and 14. H. Li contributions include research design, writing/editing, analysis, Figs. 2–5, Supplementary Figs. 2–5 and 7–10. F. Castruccio provided simulation the model and simulations description and all model data and Fig. 1 and Supplemental Figs. 11 and 12. Kyle Nardi, Dan Fu, and Xue Liu performed AR tracking, and contributed to writing/editing, and calculations and analysis necessary for the review process. Colin Zarzycki provided analysis consultations and contributed to writing/editing.

Competing interests

C.A. Shields is an associate editor for npj Climate and Atmospheric Sciences. All other authors have no competing interests.

Additional information

Supplementary information The online version contains supplementary material available at https://doi.org/10.1038/s43247-024-01774-0.

Correspondence and requests for materials should be addressed to Christine A. Shields.

Peer review information *Communications Earth & Environment* thanks the anonymous reviewers for their contribution to the peer review of this work. Primary Handling Editors: Olusegun Dada and Alireza Bahadori. A peer review file is available.